Construction and Building Materials 448 (2024) 138218

Contents lists available at ScienceDirect

Construction and Building Materials

journal homepage: www.elsevier.com/locate/conbuildmat

The effects of calcium carbonate on sodium metasilicate-activated metakaolin-based geopolymer pastes

Jie Ren [a], B. Cansu Acarturk [a], Nicolas D. Dowdy [a], Wil V. Srubar III [a,b,*]

[a] Department of Civil, Environmental, and Architectural Engineering, University of Colorado Boulder, 1111 Engineering Drive, ECOT 441 UCB 428, Boulder, CO 80309, USA

[b] Materials Science and Engineering Program, University of Colorado Boulder, 4001 Discovery Drive, Boulder, CO 80303, USA

ARTICLE INFO

Keywords:
Metakaolin
Calcium carbonate
Alkali-activation
Geopolymer
Carbonation

ABSTRACT

The influence of pure calcium carbonate ($CaCO_3$) on the alkali-activation kinetics, microstructure, and compressive strength of sodium metasilicate-activated metakaolin (MK) geopolymer cements was investigated herein. Experimental results showed that replacing 10–50 % of MK with ground $CaCO_3$ particles delayed the acceleration stage of alkali-activation regardless of replacement amount. However, 10 % $CaCO_3$ replacement increased the overall degree of reaction and yielded pastes with similar 14- and 28-day compressive strengths compared to the experimental control with no $CaCO_3$ addition. In comparison, 50 % $CaCO_3$ replacement led to a lower overall degree of reaction and lower compressive strengths through 28 days of curing. Experimental evidence substantiates that N-A-S-H gel forms in samples containing 0 % and 10 % $CaCO_3$, while N-(C)-A-S-H gel and/or C-(N)-A-S-H are also present in the binding matrix near $CaCO_3$ particles in samples with higher $CaCO_3$ contents (*i.e.*, 30 % and 50 %). While the $CaCO_3$ particles were primarily composed of calcite, vaterite, a less stable form of $CaCO_3$, was also evident in the samples containing 30 % and 50 %, suggesting that the $CaCO_3$ particles were moderately reactive during the alkali-activation. This study isolates the effects of pure $CaCO_3$ in sodium metasilicate-activated geopolymer systems, providing novel insights into its impact on geopolymerization kinetics and microstructural development for optimizing sustainable geopolymer cement formulations.

1. Introduction

Recently, scientific interest in alkali-activated metakaolin-based geopolymer cements has increased due to the global abundance of kaolinitic clays from which metakaolin (MK) is obtained [1–3] and the potential for geopolymer cements to exhibit lower environmental impacts compared to conventional portland cement [4–6]. Industrial application of geopolymer cements is not without its challenges. For example, alkali-activated MK geopolymer cements require a large quantity of highly alkaline activators to obtain satisfactory chemical compositions and properties [7]. The use of highly alkaline activators requires care and proper handling to ensure safety during mixing, placement, and finishing.

Partial replacement of MK by limestone in geopolymer cements is emerging as one of the best practice strategies for lowering the environmental impacts of geopolymer cement production and tailoring its fresh- and hardened-state properties [7–10]. Supplementing MK with limestone offers multiple benefits. First, limestone can reduce the amount of alkaline activator required to achieve a certain Si/Al and Na/Al ratio and sufficient properties, thereby lowering the environmental impacts of geopolymer cements on a per-volume basis. Second, the size of limestone particles can be adjusted to achieve desired performance characteristics. Larger particles can improve workability, while smaller particles could improve early strength due to the ball-bearing and filler effects [11]. Finally, some studies [12–14] report that limestone can provide additional nucleation sites for precipitates during geopolymerization process. In addition to providing surfaces for nucleation, a small amount of calcium (Ca^{2+}) could be liberated from limestone particles and further participate in the reaction process, forming Ca-containing N-A-S-H (*i.e.*, N-(C)-A-S-H) gels with a three-dimensional network structure. Inclusion of these gels can lead to denser microstructures and higher compressive strengths [7,15].

* Corresponding author at: Department of Civil, Environmental, and Architectural Engineering, University of Colorado Boulder, 1111 Engineering Drive, ECOT 441 UCB 428, Boulder, CO 80309, USA.
E-mail address: wsrubar@colorado.edu (W.V. Srubar III).

https://doi.org/10.1016/j.conbuildmat.2024.138218
Received 25 June 2024; Received in revised form 14 August 2024; Accepted 3 September 2024
Available online 7 September 2024

Despite a number of previous reports on the use of limestone in geopolymer cements [8–11], there is a lack of scientific understanding on how pure $CaCO_3$, the primary mineral in limestone, alters the geopolymerization kinetics, mechanical strength, and phase assemblages at early and later ages from a fundamental standpoint. Previous studies used ground limestone, which is well known to contain other minerals, such as feldspar and quartz, in addition to $CaCO_3$ [16–19]. Moreover, almost all previously studies were conducted using alkaline activating solutions containing a combination of NaOH and waterglass or sole NaOH instead of sodium silicate (i.e., Na2SiO3) alone [7,10,20–22]. Compared to NaOH, sodium silicate is much safer and, thus, potentially more feasible for industrial applications.

To address these gaps in the literature, this study systematically investigated the effects of replacing MK with pure $CaCO_3$ at different replacement levels (*i.e.*, 0 %, 10 %, 30 %, and 50 %) on the microstructure and properties of Na_2SiO_3-activated MK-based geopolymer cements. By isolating pure $CaCO_3$ as the replacement material and utilizing sodium silicate as the sole alkali activator, this research uniquely reveals how $CaCO_3$ alters the geopolymerization process. The study's comprehensive approach involved monitoring alkali activation kinetics through isothermal conduction calorimetry, testing compressive strengths at multiple curing stages (1, 3, 7, 14, and 28 days), and characterizing the resulting pastes using advanced techniques such as X-ray diffraction (XRD), thermogravimetric analysis (TGA), Fourier transform infrared spectroscopy (FTIR), and scanning electron microscopy (SEM) with energy dispersive spectroscopy (EDS). These methods provided a detailed understanding of the microstructural changes induced by CaCO3, underscoring the significance and novelty of this research in advancing the development of more sustainable and efficient geopolymer cements.

2. Materials and methods

2.1. Materials

High-purity MK powder with a specific density of 2.50 was provided by BASF Chemical Corporation (Georgia USA). Pure $CaCO_3$ powder ($\geq$ 99.0 %) with a density of 2.93 g/cm^3 was supplied by Sigma Aldrich (CAS No. 471-34-1). Anhydrous sodium metasilicate powders (SiO_2: Na_2O molar ratio at 1:1) were purchased from Sigma Aldrich (CAS No. 6834-92-0) for the preparation of the alkaline activator solution.

The MK and $CaCO_3$ were characterized using particle size analysis, X-ray fluorescence (XRF), XRD, and SEM. The D_{50} particle size of the MK and $CaCO_3$, measured by laser diffraction, was 4.76 and 19.68 μm, respectively (see Fig. 1a). The corresponding specific surface area, determined by Brunauer Emmett Teller (BET) characterization, was 11.39 m^2/g and 0.71 m^2/g for MK and $CaCO_3$, respectively. These characteristics indicate that $CaCO_3$ addition would be beneficial for workability based on its greater size and much smaller surface area. Table 1 shows the chemical composition of the MK and $CaCO_3$ determined by XRF.

Fig. 1b shows the mineralogy of the MK and $CaCO_3$ particles used herein. The data reveal that the $CaCO_3$ is mainly comprised of the calcite polymorph and trace quantities of dolomite, whereas MK exhibited a characteristic amorphous hump ranging between 15 and 30° (2θ) with traces of quartz (SiO_2) and anatase (TiO_2). Al_2O_3 was present only in the amorphous form in the MK, which is expressed as $2SiO_2{\cdot}Al_2O_3$. Thus, the total amorphous content was estimated to be 95.98 % in the MK (Al_2O_3 = 44.10 %, SiO_2 = 51.88 %) [7]. The content of anatase, quartz, and other impurities in MK was estimated to be approximately 1.54 %, 0.02 % and 2.46 %, respectively. Fig. 2 shows the morphologies of MK and $CaCO_3$ obtained from SEM in secondary electron mode. The images confirmed the average particle size for the MK (4.76 μm) and $CaCO_3$ (19.68 μm) obtained by laser diffraction (see Fig. 1a). In addition, the images show that the MK particles consisted of small, irregular, layer-shaped particles and were much smaller compared to the more angular $CaCO_3$ particles.

2.2. Experimental methods

2.2.1. Sample preparation

Sample mixture proportions are summarized in Table 2. Geopolymer paste samples contained 0 %, 10 %, 30 %, or 50 % $CaCO_3$ by mass replacement of MK. The water-to-binder ratio was held constant at 0.9 to ensure good workability. The amount of anhydrous sodium metasilicate was determined to achieve constant Si/Al and Na/Al ratios of 1.5 and 1.0, respectively. The Si/Al ratio selected is to avoid possible formation of zeolite which often occurs when the Si/Al ratio was less than 1.5 at ambient curing temperature [23,24]. In addition, this Si/Al ratio was reported to interact well with high contents of limestone, exhibiting high strength and low environmental impact [8,25]. An Na/Al ratio of 1.0 is generally beneficial for the mechanical properties and durability of the prepared specimens [26,27].

To prepare the alkaline activator solution, anhydrous sodium metasilicate was first weighed, mixed with the predetermined amount of water, and stirred in a glass beaker using a magnetic stirrer until all pellets were dissolved completely. Then, the alkaline activator was allowed to cool for 24 h at ambient conditions. A watch-glass was placed

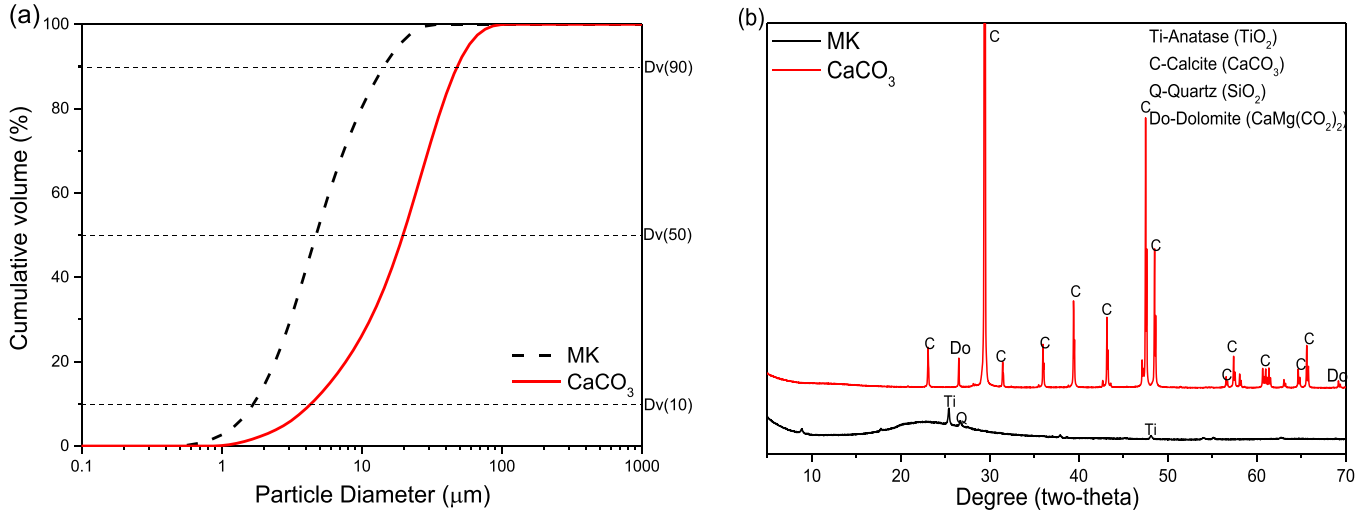

Fig. 1. (a) Particle size distribution and (b) XRD patterns of the MK and $CaCO_3$ used in this study.

Table 1
Chemical compositions (wt%) of the MK and $CaCO_3$ used in the study determined by XRF.

Raw materials	SiO_2	Al_2O_3	CaO	Fe_2O_3	Na_2O	K_2O	TiO_2	SO_3	MgO	P_2O_5	LOI
MK	51.9	44.1	0.02	0.37	0.20	0.156	1.54	0.11	0.02	0.078	1.00
$CaCO_3$	<0.07	0.21	54.9	<0.01	<0.04	0.006	0.01	0.07	0.06	0.015	41.6

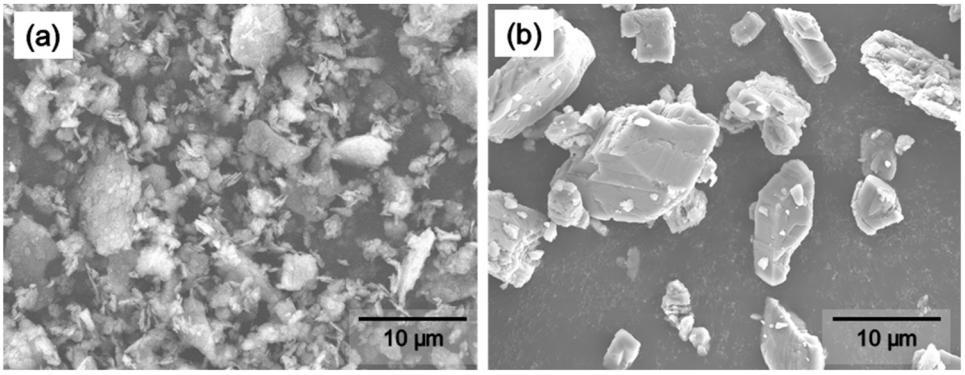

Fig. 2. SEM micrographs showing the morphologies and confirming the average particle sizes of the (a) MK and (b) $CaCO_3$ used in this study.

Table 2
Nomenclature and mixture formulations of MK-based geopolymer cement pastes.

Sample name	MK (wt%)	$CaCO_3$ (wt%)	Sodium metasilicate (wt%)	w/b ratio	Oxide-molar ratios	
					Si/Al	Na/Al
GP (Control)	100	0	52.7	0.9	1.5	1.0
GP10	90	10	47.4	0.9	1.5	1.0
GP30	70	30	36.9	0.9	1.5	1.0
GP50	50	50	26.4	0.9	1.5	1.0

on the beaker to avoid any water loss and ingress of CO_2 from the air. Then, all solid powders (*i.e.*, MK, $CaCO_3$) were weighed, mixed for 2 min at low speed in a high-shear rate mixer. Once the powders were mixed homogenously, the prepared alkaline activator was then added slowly to create a slurry. The slurry was subsequently mixed for 3 min at the highest speed. Then, the slurry was cast into 31.75 mm (1.25 in.) cubic molds and vibrated for 15 s to eliminate entrapped air. The molds were covered by a plastic film to minimize moisture loss. Samples were demolded after one day and sealed tightly in plastic bags that maintained a constant temperature of 20 ± 2 °C and relative humidity of 50–70 % until further testing.

2.2.2. Methods

The reaction kinetics of the alkali-activation of MK-based geopolymers were measured using a TAM Air isothermal calorimeter at 25 ± 2 °C for 7 days. Around 20 g of paste mixed in an ampoule was used for each mixture. The compressive strength of samples was tested after 1, 3, 7, 14 and 28 days of curing using an Instron Universal Testing machine with a displacement rate of 0.1 mm/s. The mean and standard deviation of five randomly selected specimens for each mixture were reported. After compressive strength testing, crushed pieces of 3-day and 28-day samples were collected, immersed in acetone for 24 h, then dried in a laboratory oven at 35 °C for 24 h in order to halt any further chemical reactions [7]. A small fraction of this sample was used for SEM/EDS analysis. The remainder was ground into a fine powder that was able to pass a #200 sieve (75 μm) for other characterization techniques including XRD, TGA/DTG and FTIR. XRD was carried out using a Bruker D8 ADVANCE diffractometer with Cu-Kα radiation. The X-ray beam current and acceleration voltage values were 40 mA and 40 kV, respectively. Sample powders were scanned from 5 to 70° (2θ) with a scanning rate of 1.2°/min (one step/second and 0.02°/step). TGA/DTG was carried out using an instrument (TGA5500) with a heating rate of 10 °C/min from 20 °C to 1000 °C in N_2 gas with a flow rate at around 25 ml/min. A Nicolet FTIR spectrometer was used with a resolution of 1 cm^{-1} in a range of 4000–500 cm^{-1}. Duplicate samples for each mixture were characterized. For SEM/EDS analyses, samples were first coated with platinum to improve conductivity and then observed in a high vacuum mode in secondary electron mode. The accelerating voltage was 10.0 keV and the working distance ranged around 7 mm. An elemental mapping scan was first taken to showcase the distributions of $CaCO_3$ particles. Then, approximately 20–30 EDS spectra of the binding matrix were obtained for points immediately surrounding and points further away from the $CaCO_3$ particles.

3. Results and discussion

3.1. Alkali-activation kinetics

The normalized heat flows of all freshly mixed pastes are shown in Fig. 3. The acceleration peak of the Control (denoted as 1 in Fig. 3a) shifted from about 230 min (~4 h) to about 510 min (8.5 h) in the other three mixes (denoted as 1' in Fig. 3a), suggesting a delayed geopolymerization process. The delays for the three $CaCO_3$-containing mixes were similar (~280 min), suggesting that different quantities of $CaCO_3$ addition (*i.e.*, 10 %-50 %) had no direct effect on the specific duration of retardation in the early reaction process. Upon normalization of the data by the mass of MK, some differences in normalized heat flow were evident (see Fig. 3b) compared to Fig. 3a. However, the trends were identical in terms of a reduction in the intensity of the acceleration peak, namely Control > GP10 > GP30 > GP50. This demonstrates that, with an increase in the $CaCO_3$ addition, the reaction rate of MK itself decreases. This phenomenon could be explained by a surface charge

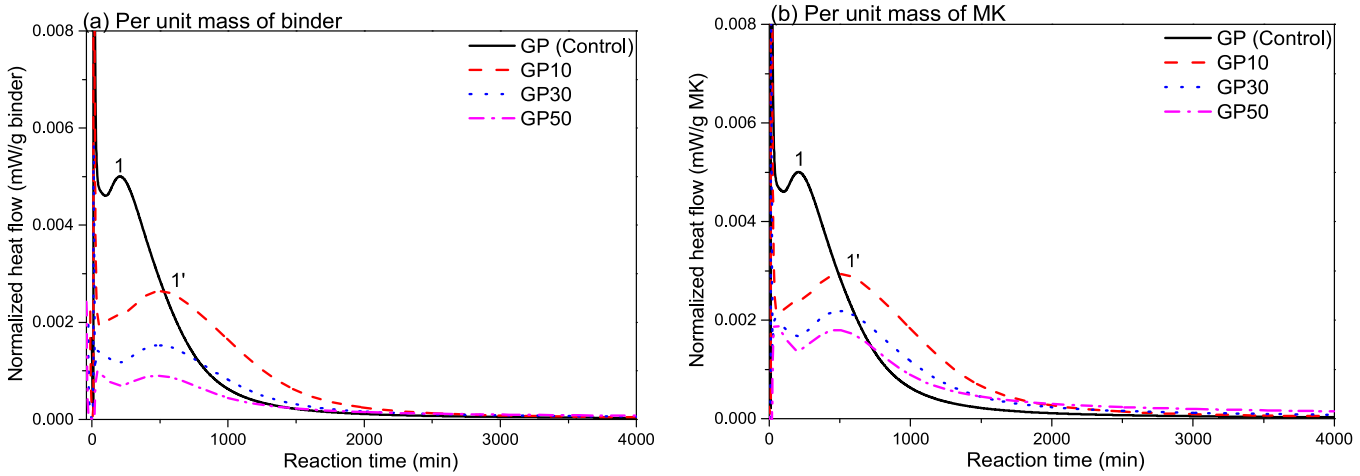

Fig. 3. Normalized heat flow per unit mass of (a) binder and (b) MK through 7 days of reaction.

effect. The surface of MK is negatively charged. However, it can become positively charged by attracting divalent Ca^{2+} liberated from $CaCO_3$ [28]. Research studies show that $CaCO_3$ can liberate Ca^{2+} and become negatively charged at pH > 13, which is representative of the pore solution pH of MK-based geopolymer binders [29,30]. With increasing $CaCO_3$ content, a larger proportion of positively charged MK particles might have interacted with the negatively charged $CaCO_3$ particles. Thus, their early alkali-activation could have been hindered to some extent, resulting in lower heat release. Another possible reason for the reduction in heat release with increasing $CaCO_3$ content is that the $CaCO_3$ is not reactive. Thus, more water was available to absorb some of the heat during alkali activation, leading to less apparent heat flow. Moreover, with a higher replacement level, the alkalinity (pH level) of the alkaline activator decreased, which could have caused a lower dissolution degree of MK particles.

According to Fig. 4a, the cumulative heat release during the first 7 days by the Control paste reached the highest value followed by GP10. In comparison, GP30 and GP50 exhibited much lower heat release, substantiating a lower degree of reaction. When the cumulative heat release is normalized by unit mass of MK (see Fig. 4b), GP10 had the largest amount of heat released after about 1420 mins (~1 day) of reaction, indicating that 10 % $CaCO_3$ facilitated the overall geopolymerization process and led to a higher degree of reaction. One explanation is that this amount of $CaCO_3$ induced a nucleation effect. Another explanation is that trace quantities of Ca^{2+} liberated by the $CaCO_3$ reacted with the silicates in the alkaline activator, thereby forming C-S-H that may also accelerate alkali-activation through a nucleation effect [31,32]. This behavior is similar to those as observed in portland cement pastes [33,34]. However, considering the relatively greater size of $CaCO_3$ and the corresponding lower intensity of the acceleration peak in Fig. 3, further investigations are required. It is also worth noting that with some $CaCO_3$ addition, the overall workability of the system was improved, leading to a better distribution for MK particles. This could also have contributed to an overall higher reaction degree. One more possible explanation is that dissolved Ca^{2+} participated in the reaction process and formed Ca-containing N-A-S-H gel (*i.e.*, N-(C)-A-S-H). Therefore, more heat could have been liberated if Ca^{2+} was involved in the geopolymerization process [32,35]. This hypothesis is further explored in Section 3.3.4.

3.2. Compressive strength

After 1-day, GP10 yielded a lower compressive strength (~8.7 MPa) than that of the Control (~15.7 MPa) but still much higher compared to the other two mixes prepared with 30 % or 50 % of $CaCO_3$ (Fig. 5). This result implies that 10 % $CaCO_3$ did not contribute to obvious filler and nucleation effects. Besides, its reactivity within one day is negligible. The compressive strength of GP30 increased to ~10.2 MPa after 3 days, which was similar to the corresponding value of GP10 (~9.3 MPa). Between 7 and 28 days, the compressive strength of the GP10 and GP30 increased at a higher rate compared to the Control. For example, the

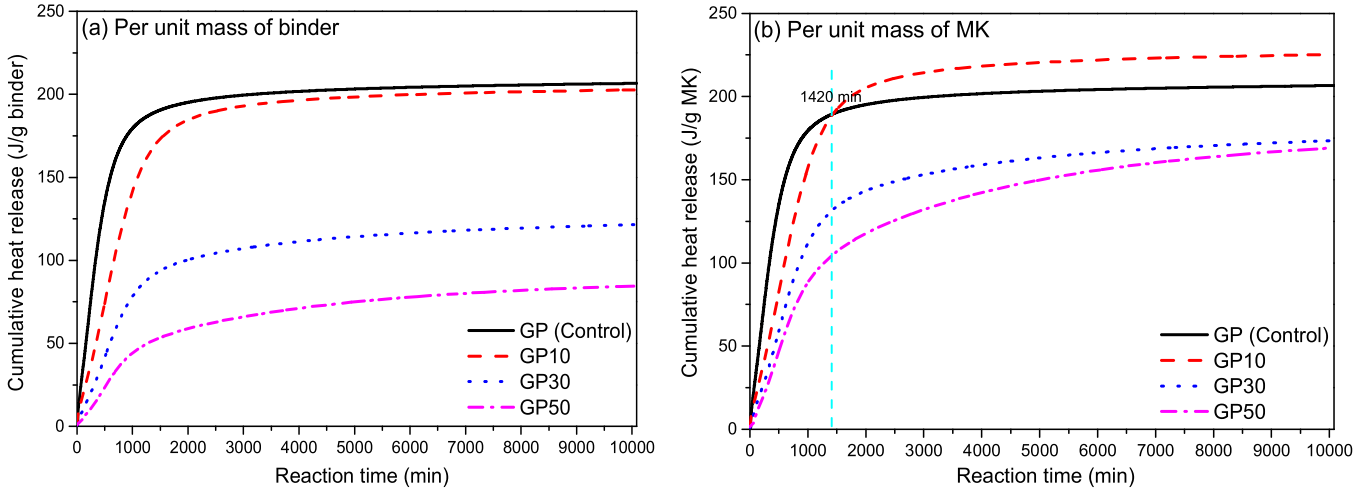

Fig. 4. Cumulative heat release during the first 7 days (10,080 mins) of reaction, (a) per unit mass of binder and (b) per unit mass of MK.

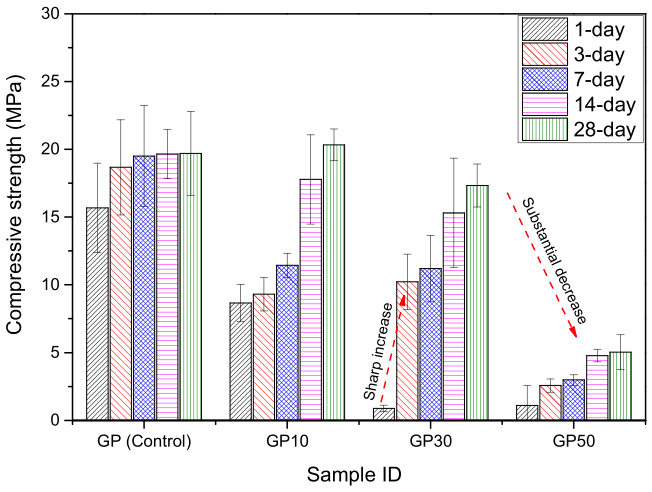

Fig. 5. Compressive strength of all mixtures after 1, 3, 7, 14, and 28 days of curing.

increase in the compressive strength of GP10 from 7 to 28 days of curing was about 77.8 % whereas for the Control, the increase was negligible. After 28 days, the compressive strengths of these two mixes were 20.3 MPa and 17.3 MPa, respectively, which were similar to the Control (19.7 MPa). In contrast, the compressive strength of GP50 was much lower among the four mixes. The strength ranged between 1.1 and 5.0 MPa throughout all curing ages.

Based on these results, it can be concluded that the addition of $CaCO_3$, regardless of dosage level, reduces the early age compressive strength, especially at 30 % and 50 % replacement. However, as curing time increased, a $CaCO_3$ replacement of 30 % led to a strength increment, with the final 28-day compressive strength similar to that of the Control specimen. However, a 50 % $CaCO_3$ dosage resulted in a loss in the compressive strength with little improvements over time. This result is consistent with another study that reported that coarse limestone powder is detrimental for compressive strength, especially at high dosage levels [36]. The increase in the compressive strength of GP30 from 1 to 3 days can be explained by considering that this amount of $CaCO_3$ (30 %) could behave as a filler with the given particle size, which helped to achieve good particle packing and lead to a fluid-to-solid transition in the binding matrix based on percolation theory [37,38]. Similarly, in another study, a $CaCO_3$ dosage of 32.1 % in a geopolymer cement formulated with Na/Al=0.96 and Si/Al=1.675 was the optimal formulation [25], which aligns with the data and conclusions obtained herein. The relatively low compressive strength for all $CaCO_3$ containing specimens at early age (within 7 days) is a limitation for these samples to be used in practical applications when high early strength is needed.

3.3. Microstructural/mineralogical characteristics

3.3.1. X-ray diffraction (XRD)

XRD patterns of the four paste specimens after 3 and 28 days of curing are shown in Fig. 6a and b, respectively. After 3 days of curing, an amorphous hump ranging between 20 and 35° 2θ (centered at 26–29° 2θ) is observed in the patterns of Control and GP10 samples, suggesting the formation of amorphous reaction products. For the other two mixtures, the amorphous hump was almost undetectable. Instead, strong peaks assigned to calcite were observed due to the introduction of $CaCO_3$ at replacement rations of 30 % or higher. Traces of crystalline phases of inert anatase (*i.e.*, TiO_2) from MK are detected in all mixtures. Similar trends can be observed after 28 days. The Control and GP10 samples exhibited high amorphous content. Based on the chemical formulas and relative content of MK and $CaCO_3$ in this study, phases such as hemi-carboaluminates ($Ca_4Al_2(OH)_{13}(CO_3)_{0.5}{\cdot}5.5H_2O$) should be present in the GP10 whereas mono-carboaluminates ($Ca_4Al_2(OH)_{12}(CO_3){\cdot}5\ H_2O$) should be present in the GP30 and GP50 samples. Due to the high intensity of the calcite peak, however, the characteristic peaks of hemi- and monocarboaluminates, which should be located at around 10.8° 2θ and 11.7° 2θ [39], could not be observed in the XRD patterns.

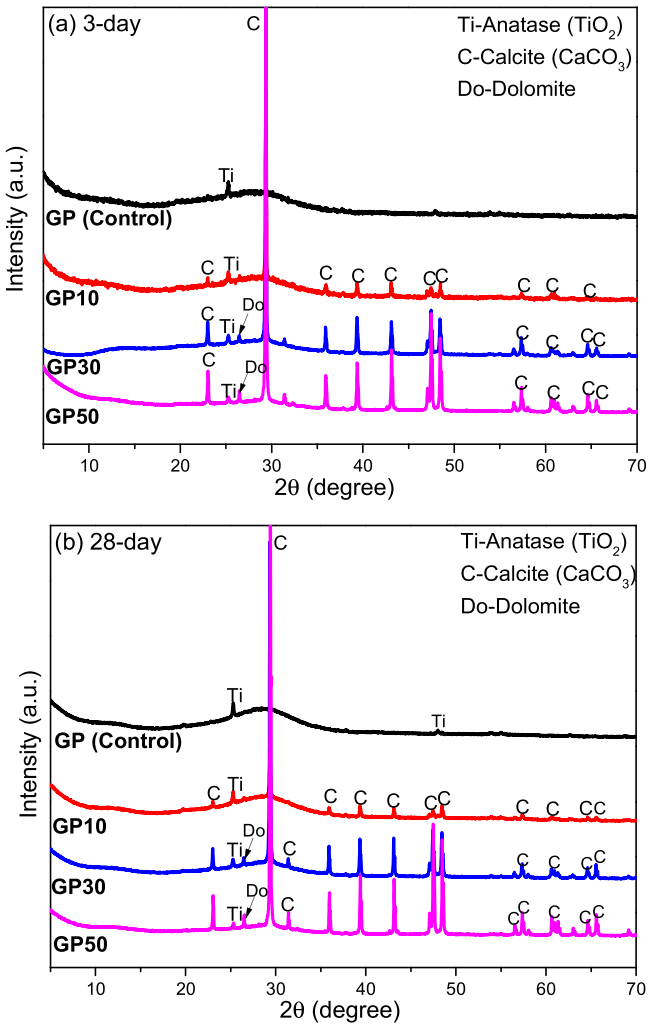

Fig. 6. XRD patterns of all mixtures after (a) 3 days and (b) 28 days of curing. Calcite peaks are truncated for ease of comparison of other peaks among different mixes.

3.3.2. Thermogravimetric analysis/derivative thermogravimetry (TGA/DTG)

The TGA curves are presented in Fig. 7. Chemically bound water is attributed to the mass loss between 105 and 550 °C [40], which can be used to estimate the total amount of hydration products. Those results are shown in Table 3. The amount of bound water decreased gradually from ~9.5 % to ~5.7 %, ~11.5–5.0 % after 3 days and 28 days, respectively, as the $CaCO_3$ addition increased. These data align with the calorimetry data in Figs. 3 and 4. that revealed higher $CaCO_3$ replacements led to lower overall degrees of reaction and, thus, the total amount of hydration products decreased. As expected, an increased amount of $CaCO_3$ addition led to greater mass loss at higher temperatures 550–800 °C, which are assigned to the decomposition of $CaCO_3$ (also shown in Table 3). The corresponding temperature at which 5 %, 10 %, and 15 % of mass loss was obtained is included in Table 3. It is obvious that with more $CaCO_3$ added (from 10 % to 50 %), the temperature also increased, which demonstrates that $CaCO_3$ improved the

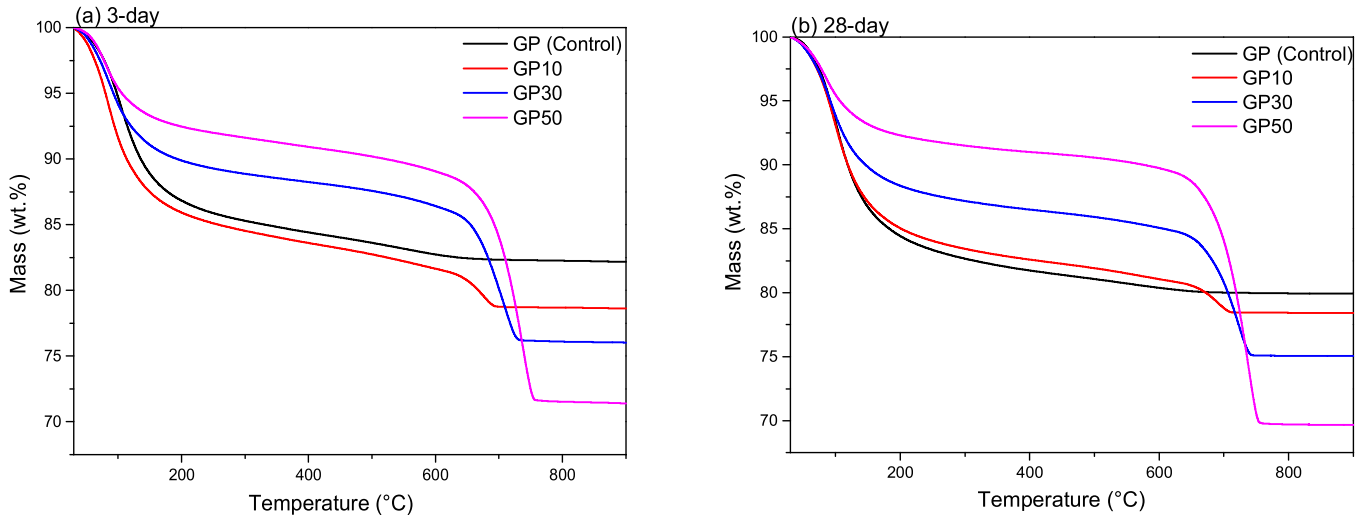

Fig. 7. TGA results of the four mixes after (a) 3 days and (b) 28 days of curing.

Table 3
Mass loss (%) for different temperature ranges and corresponding temperature values at which a certain amount of mass loss was achieved. Samples were run in duplicates.

Sample ID	3-day					28-day				
	105–550 °C	550–800 °C	T_5 (°C)	T_{10} (°C)	T_{15} (°C)	105–550 °C	550–800 °C	T_5 (°C)	T_{10} (°C)	T_{15} (°C)
GP (Control)	9.5	0.91	90.6	129.7	345.5	11.5	0.77	88.3	114.6	170.3
GP10	8.6	3.5	80.3	113.9	256.9	10.7	3.1	88.3	117.2	194.8
GP30	6.1	11.0	90.5	223.5	653.3	7.9	10.5	93.7	146.7	608.3
GP50	5.7	16.5	118.2	528.5	676.0	5.0	20.5	110.0	588.5	700.8

T_5, T_{10}, and T_{15} refers to the temperature at which 5 %, 10 % and 15 % mass loss was obtained.

thermal stability of MK-based binders. The GP50 sample exhibited an increase in the percentage of mass loss due to the decomposition of $CaCO_3$ after 28 days compared to 3 days. In comparison, GP10 and GP30 showed a slight decrease, indicating that GP50 likely underwent some degree of carbonation.

Based on the DTG curves shown in Fig. S1, higher $CaCO_3$ replacement ratios reduced the overall temperatures of decomposition of the geopolymer cement pastes between 50 and 200 °C. These peaks represent mass loss of any free or loosely physically bound water present in the binding matrix [41]. Such a shift to lower temperatures with increasing $CaCO_3$ content indicates more free and/or loosely bound water due probably to less formation of gels. In comparison, the Control sample displayed higher temperatures of decomposition, indicating more tightly bound water with more geopolymer gel formation [9]. This interpretation aligns with the observed compressive strength data, where the Control sample also exhibited higher compressive strength, intimately associated with more tightly bound water and greater gel formation. After 28 days of curing, GP50 and GP30 exhibited lower decomposition temperatures compared to the other two mixtures, again indicating a lower extent of gel formation. This result is in line with their lower compressive strength after 28 days of curing in comparison to Control and GP10 samples. Based on the Raman spectra (shown in Fig. S2), GP50 after 3 day, 28 days, and GP30 (after 28 days) exhibited some vaterite, which was not as thermally stable as calcite. This might be the reason why the corresponding temperature was lower compared to the original $CaCO_3$. Meanwhile, it also implies that part of the Ca in the $CaCO_3$ was released, reacted with CO_2 from the atmosphere (carbonation) or residual CO_3^{2-} in the pore solution and formed relatively unstable vaterite. The porous microstructure of the two samples also indicates that they were more vulnerable to carbonation, which is detrimental for long-term durability such as steel corrosion and other performances of geopolymer cements or concrete [42–45]. For GP10, more released Ca could have participated in the geopolymerization and the available CO_3^{2-} might exist in the form of Na_2CO_3 and K_2CO_3, which displayed the lowest decomposition temperature.

3.3.3. *Fourier transform infrared spectroscopy (FTIR)*

FITR method is a powerful method to characterize the Si-O-T (T: tetrahedral Si or Al) bonds in the gel structures or raw materials and the corresponding variations are reliable indicators of changes in product formation and chemical arrangement. Figs. 8 and 9 show the FTIR

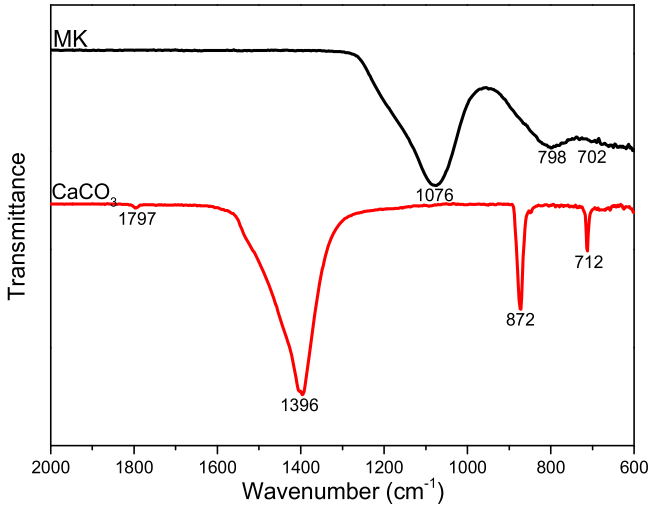

Fig. 8. FTIR spectra of MK and $CaCO_3$ before geopolymerization.

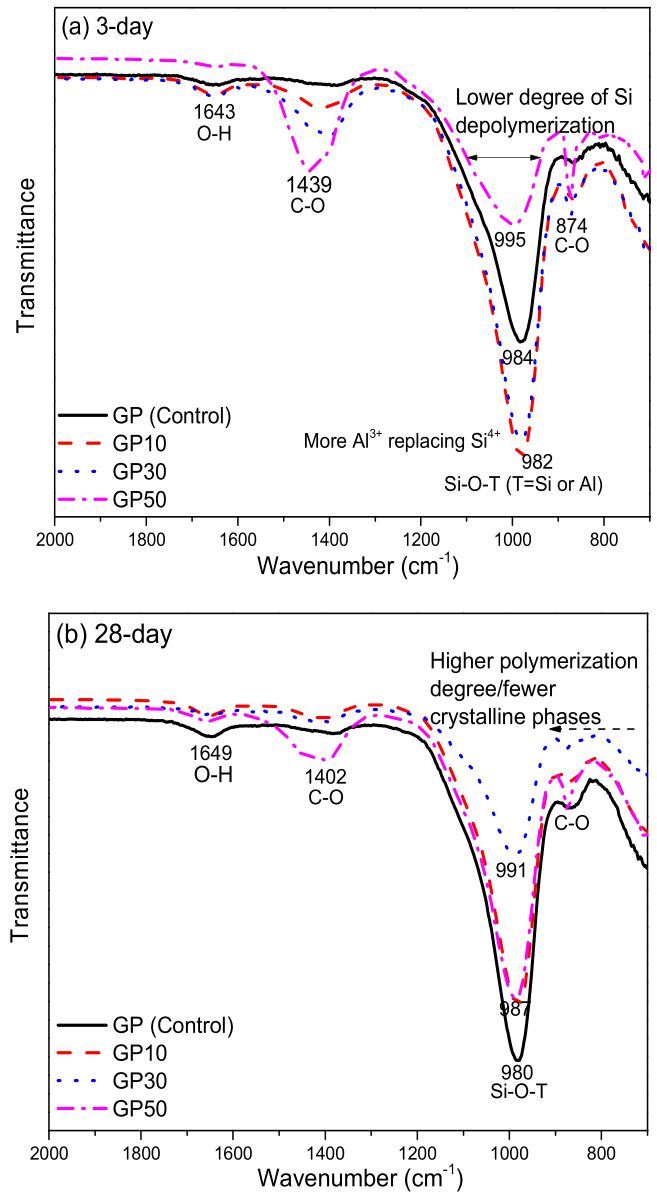

Fig. 9. FTIR spectra of the four mixes after (a) 3 days and (b) 28 days of curing.

spectra of raw materials and the four geopolymer cement pastes, respectively. For the pure MK (see Fig. 8), the band centered at around 1076 cm^{-1} indicate the presence of asymmetric stretching vibrations of Si-O-T bonds (T=tetrahedra Si or Al) [46]. The broadened bands within the range between 798 cm^{-1} and 597 cm^{-1} (not shown completely in the figure) could be attributed to the symmetric stretching of Si-O-Si bonds [47], vibrations of internal Si-O-Al oxygen bridges, as well as pseudo-lattice vibrations of small aluminosilicate rings [48]. The broadened bands also indicate amorphization of its aluminosilicate microstructure [23], corresponding well with the hump observed in the XRD patterns (see Fig. 1b). For $CaCO_3$, all bands were assigned to the asymmetric stretching of C-O-C bonds in carbonates, which belong to calcite [49].

For the geopolymer cement pastes (Fig. 8), the bands at 1643 cm^{-1} or 1649 cm^{-1} are associated with the H-OH bonds in chemically bound water in the hydrated products [50]. The bands located between 1500 and 1400 cm^{-1} and 874 cm^{-1} are related to the asymmetric C-O stretching and out-of-plan C-O bending modes respectively, implying the presence of $CaCO_3$ introduced either by the raw material or natural carbonation during the preparation process [51]. The band between 971 and 1076 cm^{-1} experienced the most significant changes, as expected. The band around 1076 cm^{-1} in MK shifted to 982–995 cm^{-1} as observed in the 3-day MK-based geopolymer samples (Fig. 9a). This shift is due to the depolymerization of the original aluminosilicate structure of the MK after the alkali-activation process [52]. Compared to the Control paste (985 cm^{-1}), the peak shifted to a higher wavenumber for the 50 % $CaCO_3$ addition (995 cm^{-1}) whereas the wavenumber shifted lower for 10 % and 30 % $CaCO_3$ replacement (~982 cm^{-1}). The higher wavenumber for GP50 suggests a lower silicate depolymerization degree. These results correspond well with the findings from another study that investigated a high percentage limestone replacement [7] and suggest that the smaller wavenumbers exhibited by the GP10 and GP30 samples might be due to the substitution of Si^{4+} by Al^{3+}, which can be promoted by some released Ca^{2+} from $CaCO_3$ [7,53]. This result indicates the possible formation of N-(C)-A-S-H gel in the mixtures due to $CaCO_3$ addition. The band at 1076 cm^{-1} gained a higher sharpness when it was located at around 977–995 cm^{-1}, indicating that the reaction products were of lower degree of disorder compared to MK but still have a general disorder as the three-dimensional aluminosilicate networks. GP50 exhibited a wider band, indicating its higher degree of disorder compared to other mixtures. This result aligns well with the other data that indicate a much lower geopolymerization degree, which could also be responsible for the lower early compressive strength of GP50 after 7 days of curing (Fig. 5). After 28 days, the location of peaks of Control at 980 cm^{-1} shifted to higher wavenumbers for GP10 and GP50 (987 cm^{-1}) and even to 991 cm^{-1} for the GP30 specimen. This result implies that with some $CaCO_3$ replacing MK, the polymerization degree was slightly higher or that fewer crystalline phases were formed.

3.3.4. Scanning electron microscopy/energy dispersive spectroscopy (SEM/EDS)

The SEM images of the four geopolymer cement pastes after 3 and 28 days of curing are shown in Fig. 10. Compared to the GP50 sample, all other mixtures, especially the Control, exhibited a relatively compact binding matrix after 3 days of curing. This finding agrees well with the 3-day compressive strength results. For the GP50 sample, the microstructure was poor with evidence of many uneven surfaces. Large $CaCO_3$ particles were covered by some loosely connected finer particles, which may be unreacted MK and/or MK with newly formed reaction products. After 28 days, both GP30 and GP10 specimens exhibited some needle-shaped reaction products with sharp edges. Similar to its microstructure at 3 days, GP50 exhibited a less densified crumbled microstructure with many fine particles loosely connected with each other.

Fig. 11a and b show the EDS-results based Ca-Al-Si and Na-Al-Si ternary atomic compositional diagrams of the reaction products, respectively, for the four mixtures after 3 days of curing. Based on the Ca distributions on the mapping images (data not shown), only points around or far away from the $CaCO_3$ particles were selected for characterization for the mixtures containing $CaCO_3$. Most data points fell within the region that belongs to N-A-S-H gel for the Control and GP10 specimens. In comparison, GP30 contained some products with lower Si but higher Ca (Point 17) and Na (Point 9), which indicate the presence of low-Ca N-A-S-H, also known as N-(C)-A-S-H, or a phase with similar elemental compositions as C-A-S-H and Ca-rich N-A-S-H (C-(N)-A-S-H). Point 38 in GP10 and Point 35 in GP50 were determined to be calcite. Points 34 and 36 are most likely indicative of C-S-H. However, these products also contained a very small amount of Al.

The 28-day EDS-results based Ca-Al-Si and Na-Al-Si ternary atomic compositional diagrams are shown in Fig. 12. After 28 days, the main hydration product was determined to be N-A-S-H gel in the Control specimen, as expected, whereas the other three mixtures displayed some phases that belong to N-(C)-A-S-H gel, likely due to liberation and participation of free Ca^{2+} in the geopolymerization process. Around the $CaCO_3$ particles, several points indicated higher Ca but lower Si contents. Compared to C-(N)-A-S-H and C-A-S-H region, these points exhibited a higher Al content. Thus, it was deduced that these points

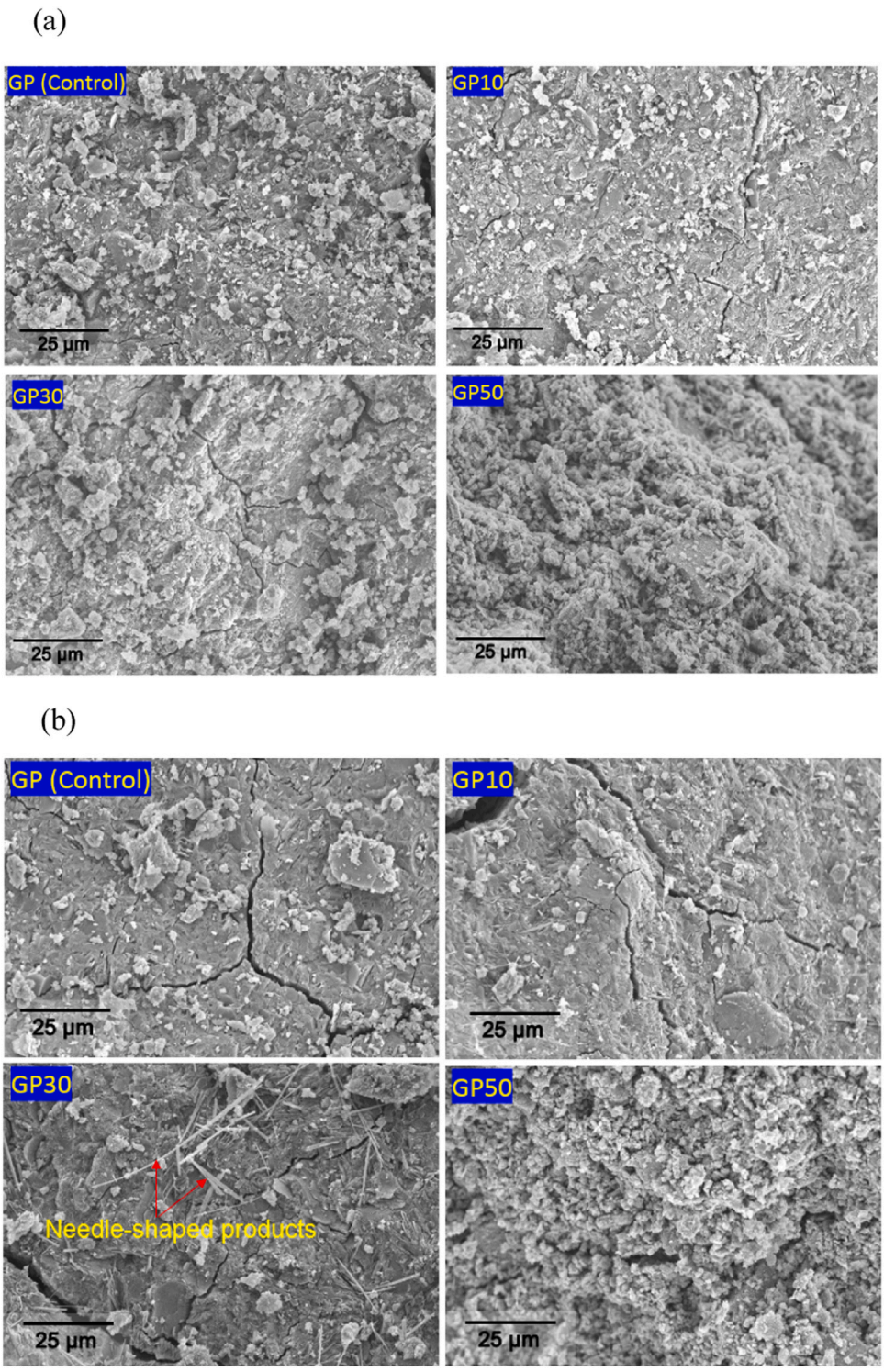

Fig. 10. SEM image of the four mixes (secondary electron mode) after (a) 3 days and (b) 28 days of curing.

indicate a combined phase of C-A-S-H, C-(N)-A-S-H, and N-(C)-A-S-H gels, which has been previously observed and reported by other studies [58–60]. GP50 exhibited some outliers (Points 9–11). These outliers indicated a high Ca/Si but lower Al content. High Ca/Si values can inhibit Al incorporation [61]. Points 37 and 47, located on the needle-shaped crystalline products, indicated a much lower Si content but higher Ca or Na content with a similar Al content compared to the other points for GP30. These needle-shaped platy phase could be Al-tobermorite [62,63] and/or efflorescence crystals due to the carbonation effect [64,65]. The corresponding elemental relative intensity and atomic ratios of Points 37 and 47 are presented in Fig. S3. Based on the general formula of Al-substituted tobermorite ($Ca_{4+x}(Al_ySi_{6-y})O_{15+2x-y}(OH)_{2-2x+y}{\cdot}5\ H_2O$) [66] and corresponding Ca/Al and Si/Al ratios, the specific chemical formula can be described as $Ca_{1.02}(Al_{2.30}Si_{3.70})O_{6.73}(OH)_{10.26}{\cdot}5\ H_2O$ (Point 37) and $Ca_{3.62}(Al_{2.70}Si_{3.30})O_{11.55}(OH)_{5.45}{\cdot}5\ H_2O$ (Point 47). Considering the existence of C and Na elements, efflorescence products, namely sodium carbonate heptahydrate ($NaCO_3{\cdot}7\ H_2O$) could have also formed. Thus, it

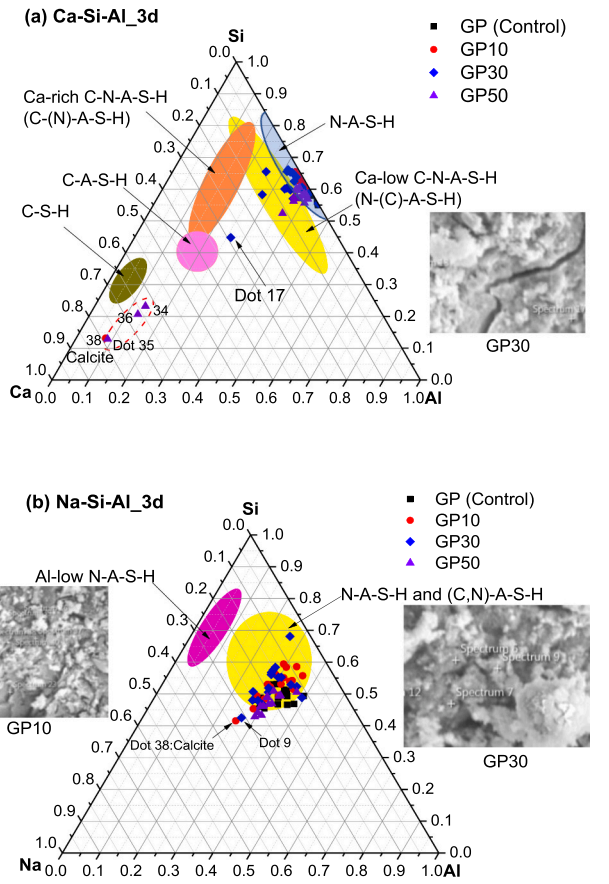

Fig. 11. Compositional ternary diagram expressed as (a) Ca-Si-Al and (b) Na-Si-Al (as normalized to 100 %) of the four mixes after 3 days of curing with corresponding phases based on previous literature [54–57].

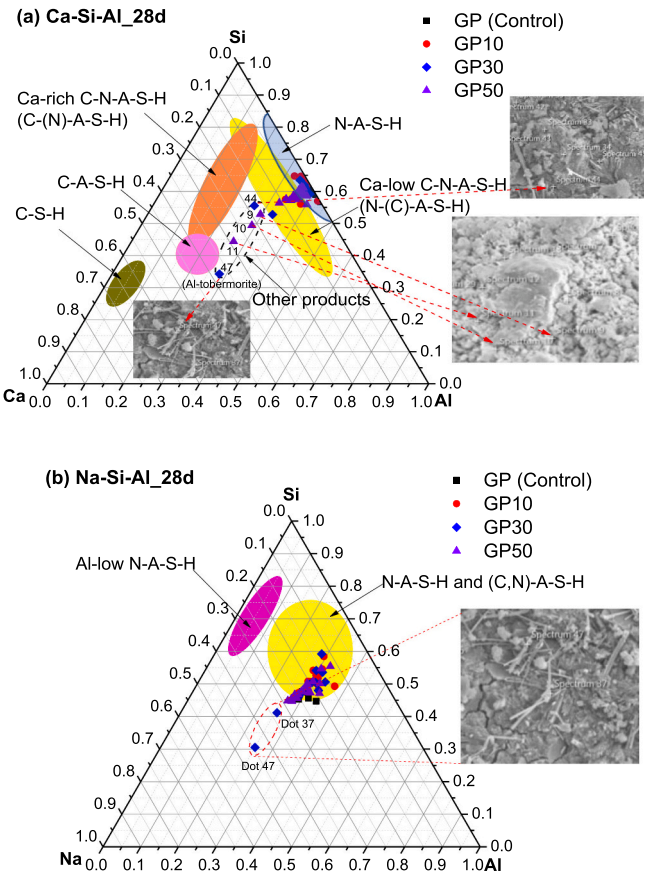

Fig. 12. Compositional ternary diagram expressed as (a) Ca-Si-Al and (b) Na-Si-Al (as normalized to 100 %) of the four mixes after 28 days of curing with corresponding phases based on previous literature [54–57].

is possible that Al-tobermorite and $NaCO_3{\cdot}7\ H_2O$ coexist, given rise to overlapping EDS measurements obtained in Points 37 and 47. No carboaluminates phases were identified, which may be an indication of a size and quantity that would be too small to be observed herein.

4. Conclusions

This study explored the effects of pure $CaCO_3$ addition on sodium metasilicate-activated MK-based geopolymer pastes in terms of hydration kinetics, mechanical strength, and microstructural development at early and later curing ages. The obtained experimental results show that industrial applications of calcium carbonates with a suitable replacement level of MK is feasible, especially when cheaper calcium carbonates are available in the future. Several main conclusions are summarized as follows:

- 10 % $CaCO_3$ promoted the overall geopolymerization reaction degree of MK-based geopolymers, as evidenced by its higher cumulative heat during the early reaction process than that of the Control.
- A 10 % $CaCO_3$ replacement led to a similar 28-day compressive strength compared to the control paste. Samples containing 30 % $CaCO_3$ exhibited very low one-day compressive strengths, but the corresponding strengths after 14 and 28 days were similar to that of the Control. Samples containing 50 % $CaCO_3$ resulted in low compressive strengths throughout the curing regime. Different results for various replacement levels can be attributed to both chemical reactivity and physical effects of $CaCO_3$ particles in the binding system.
- The $CaCO_3$ was found to be reactive during alkali-activation, especially in samples containing 30 % and 50 % $CaCO_3$ replacement. N-A-S-H gel formed in the Control paste, as well as the paste with 10 % $CaCO_3$ replacement. In contrast, samples with 30 % and 50 % $CaCO_3$ replacement exhibited a higher diversity of amorphous gels that contained Ca, such as N-(C)-A-S-H and (C)-N-A-S-H type gels, especially near $CaCO_3$ particles.
- Furthermore, there was evidence of precipitated $CaCO_3$ (*i.e.*, vaterite) in samples with 30 % and 50 % $CaCO_3$ replacement, which is indicative of the liberation and reaction of free $CaCO_3$ with atmospheric CO_2 due to the carbonation effect.

4.1. Limitations

This study used pure $CaCO_3$ instead of ground limestone to replace partial MK in order to reduce the environmental impact and improve corresponding properties. However, the pure $CaCO_3$ is not cost efficient for industrial applications and thus it is suggested to directly compare the different effects of pure $CaCO_3$ and limestone with similar particle sizes on the properties of MK-based geopolymer cements. Corresponding cost efficiency analysis of the two sources is also suggested.

CRediT authorship contribution statement

Nicolas D. Dowdy: Writing – review & editing. **B. Cansu Acarturk:** Methodology, Writing – review & editing. **Wil V. Srubar III:** Writing – review & editing, Supervision, Project administration, Funding acquisition, Conceptualization. **Jie Ren:** Writing – original draft, Methodology, Investigation, Formal analysis, Data curation, Conceptualization.

Declaration of Competing Interest

The authors declare that they have no known competing financial interests or personal relationships that could have appeared to influence the work reported in this paper.

Data availability

Data will be made available on request.

Acknowledgement

This research was made possible by the Department of Civil, Environmental, and Architectural Engineering, the College of Engineering and Applied Sciences, and the Living Materials Laboratory at the University of Colorado Boulder with financial support from the National Science Foundation (Award No. CMMI-1943554). The authors gratefully acknowledge Matthew Fyfe for his feedback and assistance with preparing and submitting this manuscript. This work represents the views of the authors and not necessarily those of the sponsors.

Appendix A. Supporting information

Supplementary data associated with this article can be found in the online version at doi:10.1016/j.conbuildmat.2024.138218.

References

[1] A.M. Rashad, Alkali-activated metakaolin: a short guide for civil Engineer–an overview, Constr. Build. Mater. 41 (2013) 751–765.
[2] X. Ke, V.A. Baki, Assessing the suitability of alkali-activated metakaolin geopolymer for thermochemical heat storage, Microporous Mesoporous Mater. 325 (2021) 111329.
[3] K. Sun, X. Peng, S. Wang, L. Zeng, P. Ran, G. Ji, Effect of nano-SiO2 on the efflorescence of an alkali-activated metakaolin mortar, Constr. Build. Mater. 253 (2020) 118952.
[4] N.B. Singh, B. Middendorf, Geopolymers as an alternative to Portland cement: an overview, Constr. Build. Mater. 237 (2020) 117455.
[5] J.L. Provis, J.S.J. Van Deventer, Geopolymers: Structures, Processing, Properties and Industrial Applications, Elsevier, 2009.
[6] J.S. Van Deventer, J.L. Provis, P. Duxson, Technical and commercial progress in the adoption of geopolymer cement, Miner. Eng. 29 (2012) 89–104.
[7] P. Perez-Cortes, J.I. Escalante-Garcia, Gel composition and molecular structure of alkali-activated metakaolin-limestone cements, Cem. Concr. Res. 137 (2020) 106211.
[8] P. Perez-Cortes, J.I. Escalante-Garcia, Design and optimization of alkaline binders of limestone-metakaolin – a comparison of strength, microstructure and sustainability with portland cement and geopolymers, J. Clean. Prod. 273 (2020) 123118.
[9] A. Cwirzen, J.L. Provis, V. Penttala, K. Habermehl-Cwirzen, The effect of limestone on sodium hydroxide-activated metakaolin-based geopolymers, Constr. Build. Mater. 66 (2014) 53–62.
[10] P. Perez-Cortes, K. Cabrera-Luna, J.I. Escalante-Garcia, Alkali-activated limestone/metakaolin cements exposed to high temperatures: structural changes, Cem. Concr. Compos. 122 (2021) 104147.
[11] J. Qian, M. Song, Study on influence of limestone powder on the fresh and hardened properties of early age metakaolin based geopolymer, in: Calcined Clays for Sustainable Concrete: Proceedings of the 1st International Conference on Calcined Clays for Sustainable Concrete, Springer, 2015, pp. 253–259.
[12] Z. Chen, H. Ye, Influence of metakaolin and limestone on chloride binding of slag activated by mixed magnesium oxide and sodium hydroxide, Cem. Concr. Compos. 127 (2022) 104397.
[13] N.R. Rakhimova, R.Z. Rakhimov, N.I. Naumkina, A.F. Khuzin, Y.N. Osin, Influence of limestone content, fineness, and composition on the properties and microstructure of alkali-activated slag cement, Cem. Concr. Compos. 72 (2016) 268–274.
[14] B. Yuan, Q. Yu, E. Dainese, H. Brouwers, Autogenous and drying shrinkage of sodium carbonate activated slag altered by limestone powder incorporation, Constr. Build. Mater. 153 (2017) 459–468.
[15] X. Gao, Q.L. Yu, H.J.H. Brouwers, Properties of alkali activated slag–fly ash blends with limestone addition, Cem. Concr. Compos. 59 (2015) 119–128.
[16] S. Columbu, M. Usai, C. Rispoli, D. Fancello, Lime and Cement Plasters from 20th century buildings: raw materials and relations between mineralogical–petrographic characteristics and chemical–physical compatibility with the limestone substrate, Minerals 12 (2) (2022) 226.
[17] H.A. de Oliveira, C.P. dos Santos, Limestone clays for ceramic industry, Clay Sci. Technol. (2020).
[18] N. Ijaz, W. Ye, Zu Rehman, Z. Ijaz, Novel application of low carbon limestone calcined clay cement (LC3) in expansive soil stabilization: an eco-efficient approach, J. Clean. Prod. 371 (2022) 133492.
[19] N. Ijaz, W.-M. Ye, Zu Rehman, Z. Ijaz, M.F. Junaid, Global insights into micro-macro mechanisms and environmental implications of limestone calcined clay cement (LC3) for sustainable construction applications, Sci. Total Environ. 907 (2024) 167794.
[20] A. Kabirova, M. Uysal, M. Hüsem, Y. Aygörmez, H. Dehghanpour, S. Pul, O. Canpolat, Physical and mechanical properties of metakaolin-based geopolymer mortars containing various waste powders, Eur. J. Environ. Civ. Eng. (2022) 1–20.
[21] A. Aboulayt, M. Riahi, M.O. Touhami, H. Hannache, M. Gomina, R. Moussa, Properties of metakaolin based geopolymer incorporating calcium carbonate, Adv. Powder Technol. 28 (9) (2017) 2393–2401.
[22] A. Aboulayt, A. Gounni, M. El Alami, R. Hakkou, H. Hannache, M. Gomina, R. Moussa, Thermo-physical characterization of a metakaolin-based geopolymer incorporating calcium carbonate: a case study, Mater. Chem. Phys. 252 (2020) 123266.
[23] M. Król, J. Minkiewicz, W. Mozgawa, IR spectroscopy studies of zeolites in geopolymeric materials derived from kaolinite, J. Mol. Struct. 1126 (2016) 200–206.
[24] P. Rożek, M. Król, W. Mozgawa, Geopolymer-zeolite composites: A review, J. Clean. Prod. 230 (2019) 557–579.
[25] P. Perez-Cortes, J.I. Escalante-Garcia, Alkali activated metakaolin with high limestone contents – statistical modeling of strength and environmental and cost analyses, Cem. Concr. Compos. 106 (2020) 103450.
[26] A. Aboulayt, M. Riahi, M. Ouazzani Touhami, H. Hannache, M. Gomina, R. Moussa, Properties of metakaolin based geopolymer incorporating calcium carbonate, Adv. Powder Technol. 28 (9) (2017) 2393–2401.
[27] P. Duxson, G. Lukey, F. Separovic, J. Van Deventer, Effect of alkali cations on aluminum incorporation in geopolymeric gels, Ind. Eng. Chem. Res. 44 (4) (2005) 832–839.
[28] M.H. Derkani, N.J. Bartlett, G. Koma, L.A. Carter, D.A. Geddes, J.L. Provis, B. Walkley, Mechanisms of dispersion of metakaolin particles via adsorption of sodium naphthalene sulfonate formaldehyde polymer, J. Colloid Interface Sci. 628 (2022) 745–757.
[29] D. Azizi, F. Larachi, M. Latifi, Ionic-liquid collectors for rare-earth minerals flotation Case of tetrabutylammonium bis (2-ethylhexyl)-phosphate for monazite and bastnäsite recovery, Colloids Surf. A: Physicochem. Eng. Asp. 506 (2016) 74–86.
[30] R. Pouhet, M. Cyr, Alkali–silica reaction in metakaolin-based geopolymer mortar, Mater. Struct. 48 (3) (2015) 571–583.
[31] A.R. Brough, A. Atkinson, Sodium silicate-based, alkali-activated slag mortars: Part I. Strength, hydration and microstructure, Cem. Concr. Res. 32 (6) (2002) 865–879.
[32] J. Ren, H. Sun, K. Cao, Z. Ren, B. Zhou, W. Wu, F. Xing, Effects of natural seawater mixing on the properties of alkali-activated slag binders, Constr. Build. Mater. 294 (2021) 123601.
[33] H. Khater, Effect of calcium on geopolymerization of aluminosilicate wastes, J. Mater. Civ. Eng. 24 (1) (2012) 92–101.
[34] S. Puligilla, X. Chen, P. Mondal, Does synthesized C-S-H seed promote nucleation in alkali activated fly ash-slag geopolymer binder? Mater. Struct. 52 (4) (2019) 65.
[35] J. Ren, H. Sun, Q. Li, Z. Li, X. Zhang, Y. Wang, L. Li, F. Xing, A comparison between alkali-activated slag/fly ash binders prepared with natural seawater and deionized water, J. Am. Ceram. Soc. 1-15 (2022).
[36] Y. Knop, A. Peled, Packing density modeling of blended cement with limestone having different particle sizes, Constr. Build. Mater. 102 (2016) 44–50.
[37] D.P. Bentz, E.J. Garboczi, Percolation of phases in a three-dimensional cement paste microstructural model, Cem. Concr. Res. 21 (2-3) (1991) 325–344.
[38] A. Boumiz, C. Vernet, F.C. Tenoudji, Mechanical properties of cement pastes and mortars at early ages: evolution with time and degree of hydration, Adv. Cem. Based Mater. 3 (3-4) (1996) 94–106.
[39] G. Puerta-Falla, M. Balonis, G. Le Saout, G. Falzone, C. Zhang, N. Neithalath, G. Sant, Elucidating the role of the aluminous source on limestone reactivity in cementitious materials, J. Am. Ceram. Soc. 98 (12) (2015) 4076–4089.
[40] I. Maruyama, E. Gartner, K. Beppu, R. Kurihara, Role of alcohol-ethylene oxide polymers on the reduction of shrinkage of cement paste, Cem. Concr. Res. 111 (2018) 157–168.
[41] S.A. Bernal, E.D. Rodríguez, R.M. De Gutiérrez, M. Gordillo, J.L. Provis, Mechanical and thermal characterisation of geopolymers based on silicate-activated metakaolin/slag blends, J. Mater. Sci. 46 (16) (2011) 5477.
[42] T.H. Vu, N. Gowripalan, P.De Silva, A. Paradowska, U. Garbe, P. Kidd, V. Sirivivatnanon, Assessing carbonation in one-part fly ash/slag geopolymer mortar: Change in pore characteristics using the state-of-the-art technique neutron tomography, Cem. Concr. Compos. 114 (2020) 103759.
[43] C. Zhao, Z. Li, S. Peng, J. Liu, Q. Wu, X. Xu, State-of-the-art review of geopolymer concrete carbonation: from impact analysis to model establishment, Case Stud. Constr. Mater. 20 (2024) e03124.
[44] S.A. Bernal, J.L. Provis, B. Walkley, R. San Nicolas, J.D. Gehman, D.G. Brice, A. R. Kilcullen, P. Duxson, J.S.J. van Deventer, Gel nanostructure in alkali-activated binders based on slag and fly ash, and effects of accelerated carbonation, Cem. Concr. Res. 53 (2013) 127–144.
[45] M.A. Longhi, Z. Zhang, B. Walkley, E.D. Rodríguez, A.P. Kirchheim, Strategies for control and mitigation of efflorescence in metakaolin-based geopolymers, Cem. Concr. Res. 144 (2021) 106431.

[46] B. Walkley, R. San Nicolas, M.-A. Sani, J.D. Gehman, J.S.J. van Deventer, J. L. Provis, Phase evolution of Na2O–Al2O3–SiO2–H2O gels in synthetic aluminosilicate binders, Dalton Trans. 45 (13) (2016) 5521–5535.
[47] J. Temuujin, K. Okada, K.J.D. MacKenzie, Effect of mechanochemical treatment on the crystallization behaviour of diphasic mullite gel, Ceram. Int. 25 (1) (1999) 85–90.
[48] W. Mozgawa, The relation between structure and vibrational spectra of natural zeolites, J. Mol. Struct. 596 (1) (2001) 129–137.
[49] C. Huang, P.F. Kerr, Infrared study of the carbonate minerals, Am. Mineral.: J. Earth Planet. Mater. 45 (3-4) (1960) 311–324.
[50] S.A. Bernal, R.M. de Gutierrez, J.L. Provis, V. Rose, Effect of silicate modulus and metakaolin incorporation on the carbonation of alkali silicate-activated slags, Cem. Concr. Res. 40 (6) (2010) 898–907.
[51] J. Zhang, C. Shi, Z. Zhang, Carbonation induced phase evolution in alkali-activated slag/fly ash cements: The effect of silicate modulus of activators, Constr. Build. Mater. 223 (2019) 566–582.
[52] W. Lee, J. Van Deventer, Use of infrared spectroscopy to study geopolymerization of heterogeneous amorphous aluminosilicates, Langmuir 19 (21) (2003) 8726–8734.
[53] S. Onutai, J. Sato, T. Osugi, Possible pathway of zeolite formation through alkali activation chemistry of metakaolin for geopolymer–zeolite composite materials: ATR-FTIR study, J. Solid State Chem. 319 (2023) 123808.
[54] J.S. van Deventer, R. San Nicolas, I. Ismail, S.A. Bernal, D.G. Brice, J.L. Provis, Microstructure and durability of alkali-activated materials as key parameters for standardization, J. Sustain. Cem. -Based Mater. 4 (2) (2015) 116–128.
[55] I. Ismail, S.A. Bernal, J.L. Provis, R. San Nicolas, S. Hamdan, J.S.J. van Deventer, Modification of phase evolution in alkali-activated blast furnace slag by the incorporation of fly ash, Cem. Concr. Compos. 45 (2014) 125–135.
[56] B. Walkley, A. Kashani, M.-A. Sani, T.D. Ngo, P. Mendis, Examination of alkali-activated material nanostructure during thermal treatment, J. Mater. Sci. 53 (2018) 9486–9503.
[57] R.J. Myers, S.A. Bernal, R. San Nicolas, J.L. Provis, Generalized structural description of calcium–sodium aluminosilicate hydrate gels: the cross-linked substituted tobermorite model, Langmuir 29 (17) (2013) 5294–5306.
[58] I. Garcia-Lodeiro, A. Palomo, A. Fernández-Jiménez, D.E. Macphee, Compatibility studies between N-A-S-H and C-A-S-H gels. Study in the ternary diagram Na2O–CaO–Al2O3–SiO2–H2O, Cem. Concr. Res. 41 (9) (2011) 923–931.
[59] Z. Chen, J.-S. Li, B.-J. Zhan, U. Sharma, C.S. Poon, Compressive strength and microstructural properties of dry-mixed geopolymer pastes synthesized from GGBS and sewage sludge ash, Constr. Build. Mater. 182 (2018) 597–607.
[60] J. Xu, A. Kang, Z. Wu, P. Xiao, Y. Gong, Effect of high-calcium basalt fiber on the workability, mechanical properties and microstructure of slag-fly ash geopolymer grouting material, Constr. Build. Mater. 302 (2021) 124089.
[61] E. Kapeluszna, Ł. Kotwica, A. Różycka, Ł. Gołek, Incorporation of Al in C-A-S-H gels with various Ca/Si and Al/Si ratio: microstructural and structural characteristics with DTA/TG, XRD, FTIR and TEM analysis, Constr. Build. Mater. 155 (2017) 643–653.
[62] B. Liu, A. Ray, P. Thomas, Strength development in autoclaved aluminosilicate rich industrial waste- cement systems containing reactive magnesia, J. Aust. Ceram. Soc. 43 (2007).
[63] R. Fernández, A.I. Ruiz, J. Cuevas, Formation of CASH phases from the interaction between concrete or cement and bentonite, Clay Miner. 51 (2) (2016) 223–235.
[64] J. Temuujin, A. van Riessen, R. Williams, Influence of calcium compounds on the mechanical properties of fly ash geopolymer pastes, J. Hazard. Mater. 167 (1) (2009) 82–88.
[65] J. Ren, H. Sun, Q. Li, Z. Li, L. Ling, X. Zhang, Y. Wang, F. Xing, Experimental comparisons between one-part and normal (two-part) alkali-activated slag binders, Constr. Build. Mater. 309 (2021) 125177.
[66] C. Biagioni, S. Merlino, E. Bonaccorsi, The tobermorite supergroup: a new nomenclature, Mineral. Mag. 79 (2) (2015) 485–495.